

ONLINE RECONSTRUCTION OF DRIFTING UNDERWATER ICE TOPOGRAPHY: THE 2D CASE

Ulrik Jørgensen and Roger Skjetne

ABSTRACT

An online estimation design for a drifting two dimensional ice topography is presented. Under the assumption that the topography can be accurately represented by a truncated Fourier series, and given a moving window of measurements along the topography, an observer design is proposed to estimate the parameters of the model. The chosen method ensures an online cutoff of higher wave numbers in the spectrum representing the topography such that sufficient data compression is achieved for transmitting the model parameters through a limited hydroacoustic communication channel. This allows online reconstruction of the underwater drifting ice topography at a remote operation center. The observer is shown to be uniformly globally exponentially stable under a persistency of excitation condition. For comparison, a design based on B-spline basis functions is also presented. The effectiveness of the estimation algorithm is verified on a set of real ice draft measurements taken from the underside of an ice sheet off the coast of Greenland.

Key Words: Ice management, sea-ice monitoring, topography mapping, online estimation, decision support, remote sensing.

I. INTRODUCTION

As ship technology and offshore operations are improving, it now becomes possible to perform complex marine operations in the far north with increased regularity. Combining this with the forecast by the United States Geological Survey [1] that approximately 30% of the world's undiscovered gas and 13% of the undiscovered oil may be located in the Arctic, this has motivated extensive research on related technological and operational challenges. As an example, [2] reports an Arctic station-keeping operation in heavy ice close to the north pole in 2004, that successfully drilled and recovered deeply buried sediments. Another example is [3], reporting a dynamic positioning (DP) operation offshore Sakhalin in 1999.

Aiming for new tools for situational awareness and better estimates of the ice-hull loads on structures operating in ice, it is of interest to develop online monitoring systems for the motion, thickness, and properties of the

sea-ice. Both above-surface and subsurface monitoring systems are relevant for these tasks. Above-surface ice properties can generally be monitored by shipboard-, aerial-, and satellite-based observations [4–6]. Focusing on estimation of ice thickness, the capabilities of these sensors to accurately measure the ice thickness or ice topography are, as reported in [7,8], limited and may not show necessary details over the desired operational area. Above-surface observations are also sensitive to weather conditions such as wind, snow, fog, and temperature, as well as icing, erosion, and darkness [9]. However, these systems have other advantages, such as a large operational range and higher capacities for communication and navigation. Underwater observation, on the other hand, has the advantages of a more stable working environment and that ice features are more distinct when seen from below [10]. The disadvantage is the general lack of infrastructure for such systems, including a sufficient level of autonomy and performance with regard to communication, navigation, and long-term operations.

Ice topography observation can either be done by a survey and post-processing of collected ice data [11,12] or by online monitoring and estimation. Examples of the first method is seen in [13], where the authors regenerate a 3D ice topography by post-processing upward looking multi-beam echo sounder (MBES) data. The data is collected by an autonomous underwater vehicle (AUV) and the result allows the identification of ice depths, cracks, and leads in the ice cover, as well as distinguishing between first- and multi-year ice. For online ice

Manuscript received July 12, 2013; revised March 31, 2014; accepted October 29, 2014.

U. Jørgensen (corresponding author, e-mail:ulrik.jorgensen@ntnu.no) and R. Skjetne (e-mail: roger.skjetne@ntnu.no) are with Centre for Autonomous Marine Operations and Systems (AMOS), Dept. of Marine Technology, Norwegian Univ. Science & Technology (NTNU), Trondheim, Norway.

Partly funded by Research Council of Norway (RCN) project 199567 "Arctic DP" with partners Kongsberg Maritime, Statoil, and DNV GL, and by RCN project 223254 "AMOS".

This is an open access article under the terms of the Creative Commons Attribution-NonCommercial-NoDerivs License, which permits use and distribution in any medium, provided the original work is properly cited, the use is non-commercial and no modifications or adaptations are made.

monitoring, [14] presents several stationary 2D upward looking sonars (ULS) that monitor the ice properties in real-time. In the case when the surface is static, the simultaneous localization and mapping (SLAM) method [15] is an alternative, and [16] has utilized this algorithm for bathymetric seabed mapping. However, the combination of online monitoring and drifting 3D underwater ice topography mapping, is an open and unsolved problem, and thus the focus of this research.

Monitoring the underwater ice topography can be arranged by either having a stationary sea bottom infrastructure, a mobile underwater sensor platform such as an AUV, or a combination of these [17]. An AUV with an upward looking MBES, as illustrated in Fig. 1, gives an increased operations area compared to a stationary system and increases its flexibility by moving freely under the ice. Challenges, on the other hand, pertain to low bandwidth underwater communication [18] and accurate navigation [19,20]. Therefore, to satisfy a limited hydroacoustic communication channel, it becomes imperative to filter and compress the large amount of data gathered by the MBES and represent the ice topography by sufficiently few parameters.

In our research we aim for a complete online 3D underwater ice topography observation system that monitors and estimates the spatially varying underwater draft of the drifting sea-ice over an operational area. This should be monitored with sufficient fidelity by one or several underwater sensors, including an AUV with an MBES, and communicated to a surface-based operations center for online decision support. As a first step towards this goal we limit our attention in this paper to the 2D case, which is to design an observer for the dynamically varying underwater sea-ice topography along a line interval based only on measurements in a moving window (emulating the AUV).

The results in this article are based on [22] where the estimation problem was first introduced. In order to strengthen the design theory, our contribution here

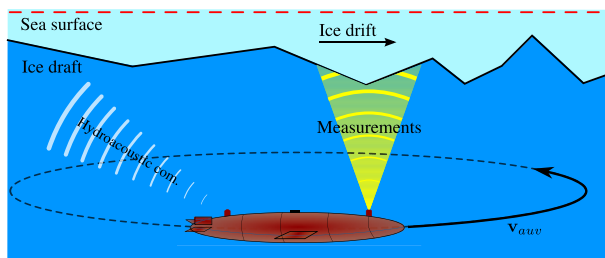


Fig. 1. AUV equipped with upward looking multi beam echo sounder, scanning the underwater ice draft [21].

includes reformulating the estimation problem into an observer-based setup by discretizing and spatially sampling the monitored interval into n nodes. We derive new important structural properties of the Fourier-based model that will substantially simplify the observer design and stability analysis. Correspondingly, we propose an observer algorithm to efficiently estimate the unknown topographic coefficients and the corresponding drafts at the nodes based only on periodic measurements along the monitored interval. Based on the overall setup and structure of this estimator system, we gain insight into stability, observability, and robustness properties of the system which will lay the foundation for an extension to the 3D case.

The proposed observer will be simulated on an unclassified ice draft data series provided by the National Snow and Ice Data Center [23]. The mission track, named SCICEX-99 (SCIENCE ICE EXERCISE [24]) and shown in Fig. 2, was collected on April 2, 1999, off the coast of Greenland during an under-ice mission by U.S. Navy submarines equipped with narrow beam sonars. The examined part is a 4km track with 1m spatial resolution and preprocessed to remove depth errors, spatial errors, and other errors.

Notation. UGES stands for Uniformly Globally Exponentially Stable. Non-bold letters are scalars, lowercase bold letters are vectors, and uppercase bold letters are matrices. The notation $f(a, b; c, d)$ indicates that a, b are fixed parameters, while c, d are variables of the function. Total time derivatives of $x(t)$ are denoted $\dot{x}, \ddot{x}, x^{(3)}, \dots, x^{(n)}$, while superscript denotes partial differentiation such that: $\alpha^b(a, b) \triangleq \frac{\partial \alpha}{\partial b}$, $\alpha^{b^2}(a, b) \triangleq \frac{\partial^2 \alpha}{\partial b^2}$ and $\alpha^{b^n}(a, b) \triangleq \frac{\partial^n \alpha}{\partial b^n}$, etc. Estimated parameters/states are denoted with a hat, i.e. \hat{z} is the estimate of z . Stacking several vectors into one is denoted $\text{col}(\mathbf{x}, \mathbf{y}, \mathbf{z}) \triangleq [\mathbf{x}^T, \mathbf{y}^T, \mathbf{z}^T]^T$. The Euclidean vector norm is $|\mathbf{x}| \triangleq \sqrt{\mathbf{x}^T \mathbf{x}}$, while the induced Euclidean matrix norm $\|\mathbf{A}\| \triangleq \sup_{\mathbf{x} \neq 0} \frac{|\mathbf{A}\mathbf{x}|}{|\mathbf{x}|}$. A matrix $\mathbf{A} \in \mathbb{R}^{n \times n}$ is called positive definite (semidefinite) and denoted $\mathbf{A} > 0$ ($\mathbf{A} \geq 0$) iff $\mathbf{x}^T \mathbf{A} \mathbf{x} > 0$ ($\mathbf{x}^T \mathbf{A} \mathbf{x} \geq 0$) $\forall \mathbf{x} \in \mathbb{R}^n \setminus \{0\}$. If $\mathbf{A} > 0$, then its smallest eigenvalue, denoted $\lambda_{\min}(\mathbf{A})$, is strictly positive. The special orthogonal group of order n is denoted by $SO(n)$.

II. PROBLEM FORMULATION

2.1 Fourier-based topographic model

Consider a typical sinusoidal time signal, written

$$\phi(t) = A \cos(\omega(t - \tau)), \quad (1)$$

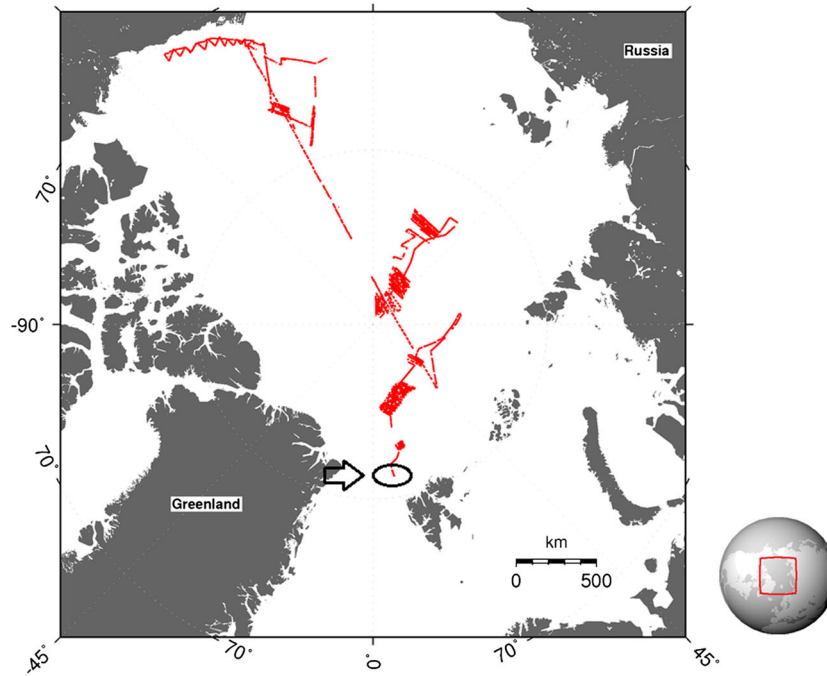


Fig. 2. Geographical location of the SCICEX-99 data series. Courtesy: NSIDC [23].

where A is the amplitude, t and τ are the time and time offset, and $\omega = 2\pi/T$ is the frequency with period T . A spatial signal is defined in the same manner as

$$\phi(s) = A \cos(\kappa(s - \xi)), \tag{2}$$

where A is the amplitude, s and ξ are the spatial parameter and displacement offset, respectively, and $\kappa = 2\pi/\lambda$ is the wave-number with wavelength λ . We see that (κ, λ) in the spatial domain is analogous to (ω, T) in the time domain, which means that methods related to sampling, approximation, and reconstruction of periodic time signals can also be used for signals in the spatial domain.

The ‘signal’ conveys information in either the time domain or spatial domain; it will generically have a propagation variable, a propagation offset, and a frequency spectrum. We let s generically represent the propagation variable, ξ the propagation offset, and κ a ‘frequency’ component. This implies that the proposed methods of this paper are also transferable to other types of signals. However, limiting our attention to topography estimation along a single spatial dimension, we model the drifting ice topography as a “propagating wave” given by a sum of sinusoidal basis functions,

$$\varphi(s) = \sum_{k=0}^p [a_k \cos k\kappa_0(s - \xi) + b_k \sin k\kappa_0(s - \xi)], \tag{3}$$

where $\kappa_0 = 2\pi/\lambda_0$ is the fundamental wave-number and λ_0 is the fundamental wavelength. Eq. 3 is recognized for $p = \infty$ as an alternative form of the Fourier series representation [25]. For p finite, let $\mathbf{c} \triangleq [a_0, a_1, \dots, a_p, b_1, \dots, b_p]^\top = \text{col}(\mathbf{a}, \mathbf{b}) \in \mathbb{R}^m$ be a constant vector with $m = 2p + 1$ coefficients corresponding to the respective wave-numbers. This yields

$$\varphi(s) = \mathbf{h}(\kappa_0, \xi, p; s)^\top \mathbf{c}, \tag{4}$$

where

$$\mathbf{h}(\kappa_0, \xi, p; s) \triangleq \begin{bmatrix} 1 \\ \cos(1 \cdot \kappa_0(s - \xi)) \\ \vdots \\ \cos(p \cdot \kappa_0(s - \xi)) \\ \sin(1 \cdot \kappa_0(s - \xi)) \\ \vdots \\ \sin(p \cdot \kappa_0(s - \xi)) \end{bmatrix} \in \mathbb{R}^m. \tag{5}$$

By discretizing the signal (4) along the spatial axis into n nodes, located at displacements $x_i, i \in \mathcal{I} \triangleq \{1, 2, \dots, n\}$, separated $\lambda_s = |x_{i+1} - x_i|$ as shown in Fig. 3, the draft of the topography at each node becomes $z_i \triangleq \mathbf{h}(\kappa_0, x_i, p; s)^\top \mathbf{c}$. For compact notation, we collect the

P3. We have $\mathbf{F}(t, s) = \mathbf{H}(s)\mathbf{C}(t)$ where by assumption $\mathbf{H}(s)$ is full row-rank, independently of s , and $\text{rank}(\mathbf{C}(t)) \geq m$ for all t . Hence, $\mathbf{F}(t, s)$ can be replaced with $\mathbf{H}(s)$ and the properties P1–P2 of Lemma 1 are still valid.

2.1.1 Wave-number analysis

To identify the ice topography (4) with sufficient precision at the same time as achieving necessary data compression, we must carefully choose the wave-numbers, that is, the numbers κ_0 and p . For this we turn to the Nyquist sampling theorem [26] that states that in order to reconstruct a time signal, this must be sampled with a frequency ω_s minimum two times faster than the highest considered frequency in the signal. Analogously, this means that a spatial signal must be sampled with a sampling wave-number κ_s minimum two times higher than the highest considered wave-number in the signal. In terms of wavelength, this corresponds to a sampling distance λ_s less than half the length of the smallest considered wavelength, that is

$$\lambda_s = \frac{2\pi}{\kappa_s} \leq \frac{1}{2} \lambda_c = \frac{\pi}{\kappa_c}, \quad (14)$$

where λ_c is the smallest considered cut-off wavelength, and κ_c is the corresponding cut-off wave-number. In (4) and (5) we see that $\kappa_p = p\kappa_0$ where κ_0 is the fundamental wave-number, found from a spectral analysis of a representable ice topography data series.

Having identified κ_c and κ_0 , we choose $\kappa_p = p\kappa_0 \geq \kappa_c$ which gives the lower bound for the integer $p \geq p_{\min} = \frac{\kappa_c}{\kappa_0}$. Then, in regard to sampling distance, we choose the upper bound $\lambda_s \leq \lambda_{s,\max} = \frac{\pi}{p\kappa_0}$, which guarantees that (14) is satisfied. Note that choosing κ_0, κ_c , and thereby p and λ_s , will influence the capability to capture the variation in the target ice topography (4) with sufficient precision. Eventually this will be a trade-off between high precision estimation and limitations in computation and the communication channel.

As illustrated in the next example, this method of fitting the topography signal to the truncated Fourier series (3) is equivalent to data compression by zeroing the wave-number components higher than κ_c in the Fast Fourier Transform (FFT) of a signal before reconstructing it through the inverse transform. Through this setup the aim is that the required data compression can be achieved without having the luxury of the complete spatial signal available for analysis (e.g. an FFT). This caters then for estimating the low wave-number part of the topography ($\kappa \leq \kappa_c$) over time with asymptotic con-

vergence of the estimation error. A further challenge is to manage this with only a partial set of nodes/samples available at each time instant through the measurements window (7).

2.1.2 Example: wave-number analysis of SCICEX-99

To determine the wave-number response of the SCICEX-99 dataset, a single sided amplitude spectrum (SSAS) of the dataset has been calculated and shown in Fig. 4. The calculated SSAS shows the energy for each wave-number in the dataset, where the second peak is identified as the fundamental wave-number $\kappa_0 \approx 0.06\text{rad/m}$ [25]. Since almost no energy is associated with wave-numbers larger than $\kappa_c = 0.6\text{rad/m}$, this is used as the cut-off wave-number. This results in the lower bound $p \geq p_{\min} = 10$. Choosing $p = 12$ gives some margin, resulting in the maximum sampling distance $\lambda_{s,\max} = 4.4\text{m}$. Hence, sampling this dataset with $\lambda_s = 1.6\text{m}$ is well within the limit.

The least-square (LS) fit of this ice topography dataset to the basis function (3) with p and κ_0 as selected above, has been computed and plotted in Fig. 5. In addition, a reconstructed signal from the inverse FFT for the entire dataset, where the wave-numbers corresponding to $\kappa \geq \kappa_c$ have been zeroed, is plotted and shown to lie on top of the LS-fitted curve. The equivalence between these two truncation methods is further substantiated

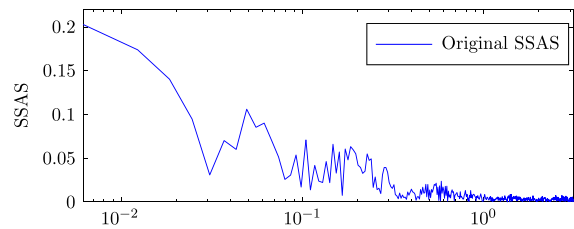


Fig. 4. SSAS of the SCICEX-99 dataset.

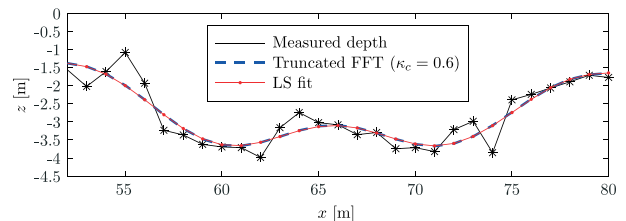


Fig. 5. A zoom-in on the SCICEX-99 ice topography dataset, incl. the curves corresponding to a least-square fit to the basis function (3) and the FFT truncated model for $\kappa \geq \kappa_c$.

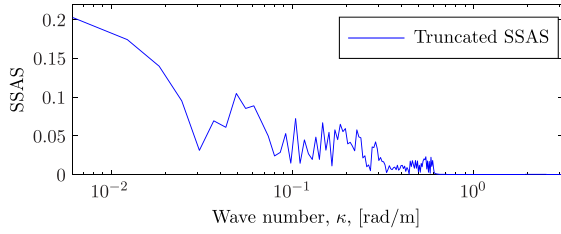


Fig. 6. SSAS of the basis function (3) LS-fitted to the SCICEX-99 dataset with p and κ_0 as selected in Example 2.1.2.

by Fig. 6, where an SSAS has been recomputed for the LS-fitted curve (3) only, showing that all wave-number components above κ_c have been eliminated.

2.2 Dynamic model for observer design

Referring to (4) and (6) as our model of the ice topography, for s constant the topography becomes stationary, while if we allow s to be dynamic the topography will become a moving surface.

For an ice field drifting with constant velocity v , the position is $s(t) = v(t - t_0) + s_0$ where s_0 is an unknown initial offset. We assume the ice drift velocity v is known, which implies an estimated displacement $\hat{s}(t) \triangleq v(t - t_0) + \hat{s}_0$, where \hat{s}_0 is a chosen initial value. Consequently, the displacement error

$$\tilde{s}(t) \triangleq \hat{s}(t) - s(t) = \hat{s}_0 - s_0 \triangleq \tilde{s}_0, \quad (15)$$

is constant, but unknown.

Using P1 of Lemma 1 we have from (15) that $\mathbf{H}(s)^\top = \mathbf{H}(\hat{s})^\top \mathbf{R}(\tilde{s})^\top$. This gives $\mathbf{z} = \mathbf{H}(\hat{s})^\top \mathbf{R}(\tilde{s})^\top \mathbf{c} = \mathbf{H}(\hat{s})^\top \mathbf{d}$, where

$$\mathbf{d} \triangleq \mathbf{R}(\tilde{s})^\top \mathbf{c} \quad (16)$$

is the coefficient vector \mathbf{c} rotated by \tilde{s} radians.

Since the true coefficients \mathbf{c} and $\mathbf{R}(\tilde{s})$ are constant, this means that also \mathbf{d} is constant. Moreover, setting $\sigma = 0$ and $\theta = -s$ in P1 of Lemma 1 and using $\mathbf{R}(-s) = \mathbf{R}(s)^\top$, then we get $\dot{\mathbf{H}} = -\mathbf{S}(v)\mathbf{H}(\hat{s}(t))$. Consequently, the underwater topographic ice model can be written

$$\dot{\mathbf{d}} = \mathbf{0} \quad \mathbf{d}(t_0) = \mathbf{d}_0 \quad (17a)$$

$$\dot{\mathbf{z}} = \mathbf{H}(\hat{s}(t))^\top \mathbf{S}(v)\mathbf{d} \quad \mathbf{z}(t_0) = \mathbf{z}_0 \quad (17b)$$

$$\mathbf{y} = \mathbf{C}(t)\mathbf{z} = \mathbf{F}(t, \hat{s}(t))^\top \mathbf{d}, \quad (17c)$$

where $\mathbf{d}_0 = \mathbf{R}(\hat{s}_0 - s_0)^\top \mathbf{c}$, $\mathbf{z}_0 = \mathbf{H}(s_0)^\top \mathbf{c} = \mathbf{H}(\hat{s}_0)^\top \mathbf{d}_0$, and the coefficient vector \mathbf{d} is unknown and subject to estimation.

Since the s -dynamics is hidden within the sinusoidal functions of $\mathbf{R}(s)$, we cannot observe and reconstruct s directly from \mathbf{y} or \mathbf{z} . However, due to the reformulation in (16) this is not important as long as an accurate ice drift velocity estimate \hat{v} is provided. On the other hand, the next lemma will, under a persistency of excitation (PE) condition show that it is possible to observe the coefficient vector \mathbf{d} from only a subset of the draft measurements \mathbf{z} available at each time instant.

Lemma 2. Suppose there exist positive constants α_0, α_1 , and T_0 such that

$$\alpha_0 \mathbf{I} \leq \int_t^{t+T_0} \mathbf{F}(\tau, s(\tau))\mathbf{F}(\tau, s(\tau))^\top d\tau \leq \alpha_1 \mathbf{I}, \quad (18)$$

for all $t \geq 0$. Then the subsystem (17a) with output (17c) is uniformly completely observable (UCO) [27].

Proof. Since the transition matrix for (17a) is the identity matrix, the PE integral (18) becomes equal to the observability Gramian for the subsystem (17a), (17c). UCO then follows by its definition [27].

The right-hand inequality of (18) is always satisfied since $\mathbf{F}(t, s)$ is absolutely continuous a.e. and bounded. In the case where the number of currently measured nodes is $n_m(t) = \text{rank}(\mathbf{C}(t)) \geq m$, then $\mathbf{F}(t, s)\mathbf{F}(t, s)^\top$ is strictly positive by Lemma 1, and the left-hand inequality of (18) is trivially satisfied. However, the PE integral (18) allows for a weaker condition, in that

$$\mathbf{F}(t, s)\mathbf{F}(t, s)^\top = \sum_{i=1}^n c_i(t)\mathbf{h}(\kappa_0, x_i, p; s)\mathbf{h}(\kappa_0, x_i, p; s)^\top \quad (19)$$

can be singular pointwise in time, but builds rank over time. For the perfect model (3), it can be shown to be sufficient to measure only one node, e.g. Node 1, to build up full rank for the PE condition as long as the speed v is nonzero. Higher speed or more measurements will increase this observability rate and robustify it for real world application.

2.3 Problem statement

We suppose that an underwater mobile sensor is operated to repeatedly scan the draft at the nodes $x_i, i \in \mathcal{I}$, through the measurements window (7) with a nonzero relative speed between the ice drift and the mobile sensor. Let $\hat{\mathbf{z}}$ be the estimate of the topographic model (6). The

objective is to design an ice topography estimator based on the model (17) with time-varying measurement vector (17c), that is, an asymptotically stable observer such that

$$\lim_{t \rightarrow \infty} |\hat{\mathbf{z}}(t) - \mathbf{z}(t)| = \mathbf{0}. \quad (20)$$

By construction and based on the Nyquist sampling theorem, this will give a continuous approximation to the topography of the drifting ice field in the specified operations area (interval) with a sufficiently limited online communication demand of signal parameters.

III. TOPOGRAPHIC ESTIMATOR DESIGN

Given the formulation of the previous section, the topography observer design is based on (17), excluding (17b), resulting in the model

$$\dot{\mathbf{d}} = \mathbf{0} \quad \mathbf{d}(t_0) = \mathbf{d}_0 \quad (21a)$$

$$\mathbf{y} = \mathbf{C}(t)\mathbf{z} = \mathbf{F}(t, \hat{s}(t))^\top \mathbf{d}, \quad (21b)$$

where we assume that $\mathbf{F}(t, \hat{s}(t))$ satisfies the PE condition (18).

3.1 Fourier-based observer design

Let $\hat{\mathbf{d}} \in \mathbb{R}^m$ and $\hat{\mathbf{y}} \in \mathbb{R}^n$ be estimates of \mathbf{d} and \mathbf{y} , respectively. Various observer designs are now possible to estimate the coefficient vector (21a), for instance some Bayesian filtering technique such as Kalman or particle filters. However, choosing a deterministic design for simplicity, we use the estimated output vector

$$\hat{\mathbf{y}} \triangleq \mathbf{F}(t, \hat{s}(t))^\top \hat{\mathbf{d}}, \quad (22)$$

as part of an injection term motivated by a gradient algorithm [28] to minimize the cost function

$$\begin{aligned} J(t, \hat{\mathbf{d}}, \mathbf{d}) &= \frac{1}{2} (\hat{\mathbf{y}}(t) - \mathbf{y}(t))^\top \mathbf{W} (\hat{\mathbf{y}}(t) - \mathbf{y}(t)) \\ &= \frac{1}{2} (\hat{\mathbf{d}} - \mathbf{d})^\top \mathbf{F}(t, \hat{s}(t)) \mathbf{W} \mathbf{F}(t, \hat{s}(t))^\top (\hat{\mathbf{d}} - \mathbf{d}), \end{aligned} \quad (23)$$

where $\mathbf{W} = \mathbf{W}^\top > 0$. Accordingly, we propose the coefficient observer

$$\begin{aligned} \dot{\hat{\mathbf{d}}} &= -\mathbf{L}_d \mathbf{J}^{\hat{\mathbf{d}}}(t, \hat{\mathbf{d}}, \mathbf{d})^\top \\ &= -\mathbf{L}_d \mathbf{F}(t, \hat{s}(t)) \mathbf{W} \tilde{\mathbf{y}}, \quad \hat{\mathbf{d}}(t_0) = \hat{\mathbf{d}}_0, \end{aligned} \quad (24)$$

where $\tilde{\mathbf{y}} \triangleq \hat{\mathbf{y}} - \mathbf{y}$ is the output error and $\mathbf{L}_d = \mathbf{L}_d^\top > 0$ is a gain matrix to tune the rate of adaptation of the individual coefficients in $\hat{\mathbf{d}}$. A good choice of \mathbf{L}_d can be selected if a representative amplitude spectrum of the area is

known in advance, as the most important wave numbers to estimate are the wave numbers that have the largest amplitude in the amplitude spectrum. The adaptation gain matrix \mathbf{L}_d can then be chosen accordingly to emphasize the corresponding coefficients. If no knowledge of the operating area is known in advance, the coefficients of the smallest wave numbers are generally most important.

From (17) and (24) we get the error dynamics

$$\dot{\tilde{\mathbf{d}}} = -\mathbf{L}_d \mathbf{F}(t, \hat{s}(t)) \mathbf{W} \mathbf{F}(t, \hat{s}(t))^\top \tilde{\mathbf{d}}, \quad (25)$$

where $\tilde{\mathbf{d}} \triangleq \hat{\mathbf{d}} - \mathbf{d}$.

Theorem 1. Suppose $\mathbf{F}(t, s)$ satisfies the PE condition of Lemma 2. Then there exist strictly positive constants α and β such that the solutions of (25), for all $0 \leq t_0 \leq t$, satisfy

$$|\tilde{\mathbf{d}}(t)| \leq \alpha |\tilde{\mathbf{d}}(t_0)| e^{-\beta(t-t_0)}, \quad (26)$$

that is, the equilibrium $\tilde{\mathbf{d}} = \mathbf{0}$ is UGES.

Proof. There exist a lower triangular matrix $\mathbf{N} > 0$ such that $\mathbf{W} = \mathbf{N}\mathbf{N}^\top$. Hence, $\dot{\tilde{\mathbf{d}}} = -\mathbf{L}_d \mathbf{Q}(t) \mathbf{Q}(t)^\top \tilde{\mathbf{d}}$ where $\mathbf{Q}(t) \triangleq \mathbf{F}(t, \hat{s}(t)) \mathbf{N}$. We have $\forall t \geq 0$ that $\mathbf{Q}(t) \mathbf{Q}(t)^\top \geq 0$ and, from Lemma 1 (P2, P3), that $\exists \mu > 0$ such that $\|\mathbf{Q}(t)\| \leq \mu$. Setting $\mathbf{P} = \frac{1}{2} \mathbf{L}_d^{-1}$ and $\mathbf{K}(t) = \mathbf{L}_d \mathbf{Q}(t)$, then all requirements of [27, lemma 1 and lemma 2] are satisfied. This concludes that (25) is UGES, which by definition implies (26).

As a result of Theorem 1, the observer error $\tilde{\mathbf{d}}(t)$, and thus $\tilde{\mathbf{z}}(t) \triangleq \hat{\mathbf{z}}(t) - \mathbf{z}(t) = \mathbf{H}(\hat{s}(t))^\top \tilde{\mathbf{d}}(t)$, will converge exponentially to zero with convergence rate β , and the goal (20) is obtained. Increasing \mathbf{L}_d or \mathbf{W} will increase the convergence rate on the cost of a more aggressive and noise-sensitive observer. Since T_0 is the minimum time it takes to achieve full rank in (18), an increased T_0 will reduce the convergence rate. T_0 depends on the number of parameters m , the fundamental wave-number κ_0 , and the relative speed between the ice topography and the underwater sensor.

3.1.1 Robustness with respect to uncertainties

In the previous sections we have made the strong assumption that the ice drift speed is constant and known, and that there is no noise in the measurement. However, since the error dynamics is UGES, we get for free that it is also input-to-state stable (ISS), given a global Lipschitz condition [29, lemma 4.6].

Suppose that \hat{v} is our estimate of the true drift speed v such that $\tilde{s}(t) = \tilde{v}(t - t_0) + \tilde{s}_0$ where $\tilde{v} \triangleq \hat{v} - v$. Then $\mathbf{d}(t) = \mathbf{R}(\tilde{s}(t))^\top \mathbf{c}$ is time-varying, but bounded with fixed length equal to \mathbf{c} .

Moreover, assume that each measured positions $x_i, i \in \mathcal{I}$ is affected by an error $\delta_x \sim \mathcal{N}(0, \sigma_x^2)$. We then get the draft

$$z_i = \mathbf{h}(\kappa_0, x_i + \delta_x, p; s)^\top \mathbf{c} \quad (27)$$

$$= \mathbf{h}(\kappa_0, x_i, p; s + \delta_x)^\top \mathbf{c}, \quad (28)$$

which gives

$$\mathbf{z} = \mathbf{H}(s + \delta_x)^\top \mathbf{c} = \mathbf{H}(s)^\top \mathbf{R}(\delta_x) \mathbf{c}, \quad (29)$$

where $\mathbf{R}(\delta_x) \mathbf{c} \sim \mathcal{N}(\mathbf{c}, \sigma_c^2)$ is bounded with fixed length equal to \mathbf{c} and $\sigma_c = \mathbf{R}(\sigma_x) \mathbf{c}$. For all measurements we have that

$$\begin{aligned} \mathbf{y} &= \mathbf{C}(t) \mathbf{z} = \mathbf{C}(t) \mathbf{H}(s)^\top \mathbf{R}(\delta_x) \mathbf{c} \\ &+ \mathbf{C}(t) \mathbf{H}(s)^\top \mathbf{c} - \mathbf{C}(t) \mathbf{H}(s)^\top \mathbf{c}, \end{aligned} \quad (30)$$

which gives

$$\mathbf{y} = \mathbf{F}(t, \hat{s})^\top \mathbf{d} + \mathbf{v}_y, \quad (31)$$

where $\mathbf{v}_y = \mathbf{C}(t) \mathbf{H}(s)^\top (\mathbf{R}(\delta_x) - \mathbf{I}) \mathbf{c}$ can be considered bounded zero mean Gaussian white noise. Hence, (31) can be considered a general measurement equation where \mathbf{v}_y is bounded measurement noise.

The observer error dynamics then become

$$\begin{aligned} \dot{\tilde{\mathbf{d}}} &= -\mathbf{L}_d \mathbf{F}(t, \hat{s}) \mathbf{W} \mathbf{F}(t, \hat{s})^\top \tilde{\mathbf{d}} \\ &+ \mathbf{S}(\tilde{\mathbf{v}}) \mathbf{d}(t) + \mathbf{L}_d \mathbf{F}(t, \hat{s}) \mathbf{W} \mathbf{F}_y(t) \end{aligned} \quad (32)$$

where we used that $\dot{\mathbf{R}}(\tilde{s}) = \mathbf{R}(\tilde{s}) \mathbf{S}(\tilde{\mathbf{v}})$. As the “disturbances” $\mathbf{d}(t)$ and $\mathbf{v}_y(t)$ enter additively through uniformly bounded matrices, the system is ISS with respect to these disturbances.

The observer also has a typical lowpass characteristics with attenuation of high frequency measurement noise. In addition, simulations show low sensitivity to discrepancies in $\tilde{\mathbf{v}}$, as further discussed in Section IV.

3.1.2 Simulation

To verify the convergence properties of the Fourier-based estimator, a simulation has been done on an ideal sinusoidally shaped topography (3). The time evolution of the normalized cost function

$$J_0(t) = \frac{\tilde{\mathbf{z}}(t)^\top \mathbf{W} \tilde{\mathbf{z}}(t)}{\sup_{t \geq 0} \tilde{\mathbf{z}}(t)^\top \mathbf{W} \tilde{\mathbf{z}}(t)}, \quad (33)$$

is used to quantify the convergence rate of the node estimates. To show that also the coefficient estimates converge, we plot the time evolution of

$$J_d(t) = \frac{\tilde{\mathbf{d}}(t)^\top \tilde{\mathbf{d}}(t)}{\sup_{t \geq 0} \tilde{\mathbf{d}}(t)^\top \tilde{\mathbf{d}}(t)}. \quad (34)$$

The topography is given by (3), with $p = 10, \kappa_0 = \pi/10$ rad/m, $v = 1.0$ m/s, the $p + 1$ elements in \mathbf{a} are evenly distributed between -5.5 and -0.5 , and $\mathbf{b}^\top = [1, \dots, 1]$. The sampling distance is $\lambda_s = 0.8$ m, the gains were set to $\mathbf{L}_d = 0.1 \cdot \mathbf{I}$ and $\mathbf{W} = \mathbf{I}$, and the initial conditions were $\hat{s}_0 = -2$ m, $s_0 = 0$ m, and $\hat{\mathbf{d}}(0) = \mathbf{0}$ m.

For this simulation, the interval of measured nodes according to (7), was set fixed within $[1.5 \text{ m}, 7.5 \text{ m}]$, enveloping a total of 8 nodes as indicated by the blue stems in Fig. 7. This emulates a stationary sensor instead of a mobile sensor, and illustrates the observability property of the system with less measured nodes than coefficients to estimate.

Three different time instants of the simulation are shown in Fig. 7, while the performance according to (33) and (34) are shown in Fig. 8. The simulation verifies the exponential convergence according to Theorem 1. Note

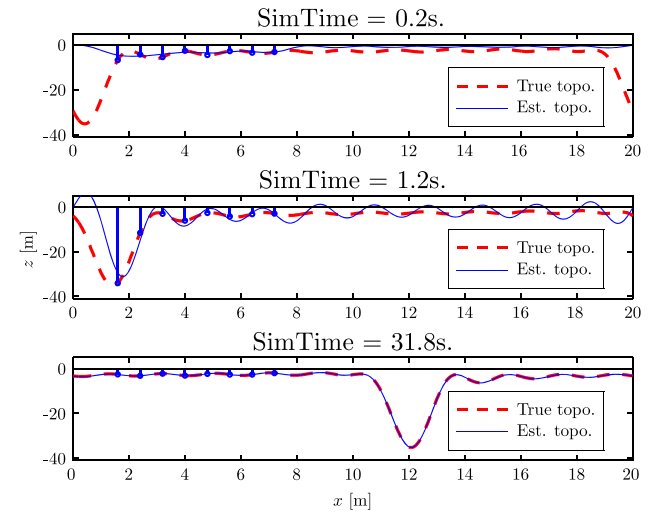


Fig. 7. Three time instants of the ideal topography. The blue stems represent the non-moving draft measurements \mathbf{y} .

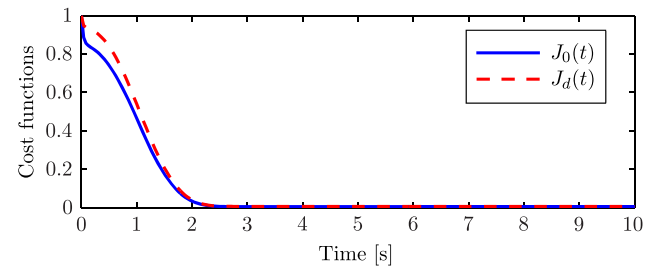


Fig. 8. Time evolutions of estimation error according to (33) and (34).

especially in the second plot of Fig. 7, the rapid convergence when the most significant part of the wave is measured. Faster convergence will generally be attained if the ice speed v is higher, since the system then experiences a higher level of excitation.

3.2 B-spline-based observer design

To analyze the performance of the observer, we will compare the Fourier-based design to an observer based on B-splines. A B-spline model is chosen because of important properties such as local support, smoothness, continuity, positivity, and simple derivatives [30]. Especially the local support property distinguishes the B-splines from the Fourier basis.

According to [30] the B-spline ϕ_j^{d+1} of degree d and order $d + 1$ with knots $k_j < \dots < k_{j+d+1}$ is defined recursively as

$$\phi_j^{d+1}(x) \triangleq \frac{x - k_j}{k_{j+d} - k_j} \phi_j^d(x) + \frac{k_{j+d+1} - x}{k_{j+d+1} - k_{j+1}} \phi_{j+1}^d(x), \quad (35)$$

where the initial B-spline of order one is defined as

$$\phi_j^1(x) \triangleq \begin{cases} 1, & \text{if } x \in [k_j, k_{j+1}) \\ 0, & \text{else.} \end{cases} \quad (36)$$

We model the underwater ice topography as a linear combination of the $m = p + d$ B-spline basis functions ϕ_j^d for $j \in [-d, p - 1]$, that is

$$\sigma(\xi; s, \mathbf{d}) = \sum_{j=-d}^{p-1} d_j \phi_j^d(s - \xi), \quad (37)$$

where d_j are the coefficients (or weights) of the B-splines. Hence, the topography $\sigma(\xi; s, \mathbf{d})$ can be written in vector form $\sigma(\xi; s, \mathbf{d}) = \mathbf{h}(\xi; s)^\top \mathbf{d}$, where $\mathbf{d} \triangleq \text{col}(d_{-d}, \dots, d_{p-1}) \in \mathbb{R}^m$ and

$$\mathbf{h}(\xi; s) \triangleq \text{col}(\phi_{-d}^d(\xi - s), \dots, \phi_{p-1}^d(\xi - s)) \in \mathbb{R}^m. \quad (38)$$

Discretizing (37) as in Section 2.1 yields the draft vector

$$\mathbf{z} = \mathbf{H}(s)^\top \mathbf{d}, \quad \mathbf{H} : \mathbb{R} \rightarrow \mathbb{R}^{m \times n}, \quad (39)$$

where $\mathbf{H}(s) \triangleq [\mathbf{h}(x_1; s), \dots, \mathbf{h}(x_n; s)]$. Eq. 39 is in the same form as (6) and the B-spline is therefore an equivalent basis for the problem of ice topography estimation. As a result, the same update law as in (25) can be used to update the coefficient estimates $\hat{\mathbf{d}}$.

3.2.1 Simulation

To verify the performance of the B-spline method, a simulation has also been conducted on an ideal B-spline shaped topography based on (37). The setup was the same as in Section 3.1.2, with $d = 3, m = 11$, and $\mathbf{d} = -\text{col}(\mathbf{0}_3, 2, 1, 3, 1, 4, \mathbf{0}_3)$. The gains were chosen as $\mathbf{L}_d = 20 \cdot \mathbf{I}$ and $\mathbf{W} = \mathbf{I}$, while $\hat{s}_0 = s_0 = 20$ m, and $\hat{\mathbf{d}}(0) = \mathbf{0}$. The measurement region was again set fixed, now at [12 me, 18 me] due to the local characteristics of the B-splines. The $N_k = m + d + 1$ knots were distributed evenly between [-7.5 m, 27.5 m]. The result of the simulation is seen in Fig. 9–10, demonstrating that the estimation errors converge as expected.

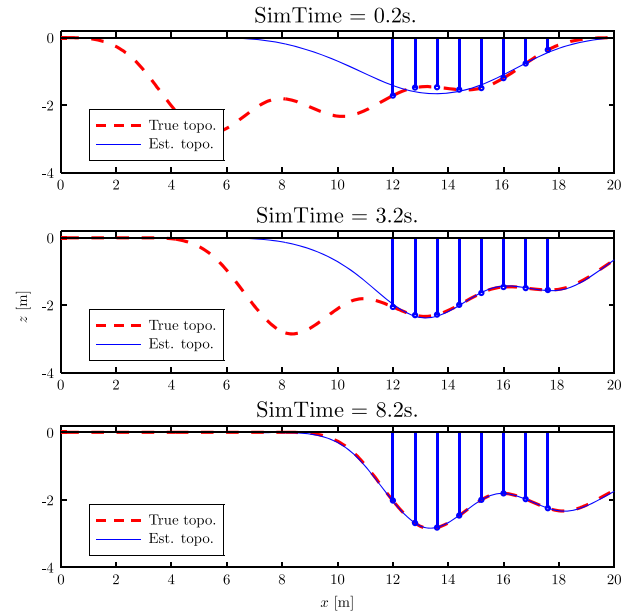


Fig. 9. Three time instants of the B-spline topography. The blue stems represent the fixed draft measurement window \mathbf{y} .

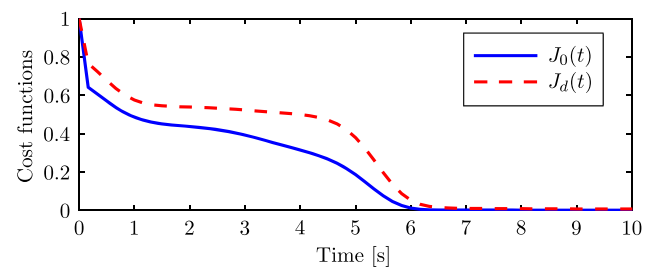


Fig. 10. Estimation errors according to (33) and (34).

IV. CASE STUDY

For a real case study we consider the SCICEX-99 dataset presented in the introduction. Appropriate values for κ_0, κ_c, p , and λ_s were found in Section 2.1.2 to be $p = 12, \kappa_0 = 0.06 \text{ rad/m}, \kappa_c = 0.6 \text{ rad/m}$, and $\lambda_s = 1.6 \text{ m}$, giving $m = 2p + 1 = 25$ coefficients to estimate. A monitoring region was specified to the interval $[0 \text{ m}, 50 \text{ m}]$, with $n = 31$ measurement nodes distributed evenly along it. The matrix \mathbf{L}_d was diagonal with m evenly distributed diagonal elements from 1.00 to 0.04, prioritizing the most important coefficients as explained in Section 3.1. Other parameters were set as in Section 3.1.2.

For comparison, the B-spline method was also tested, with $d = 3, p = 22, N_k = p + 2d + 1$ knots distributed evenly in $[-7 \text{ m}, 57 \text{ m}]$, and $\mathbf{L}_d = 20 \cdot \mathbf{I}$. The number of coefficients to estimate is $m = d + p = 25$.

To emulate an AUV with an upward-looking MBES (see Fig. 1), we simply let the measurement window (7) move along the horizontal axis with velocity $v_{auv} = 5.0 \text{ m/s}$ from its initial region at $[5 \text{ m}, 15 \text{ m}]$. In a real experiment, the velocity of the AUV would not be perfectly constant. However, this is not critical to the observer performance as long as a nonzero relative velocity between the AUV and ice cover is attained (since Lemma 2 then will be satisfied nonetheless). It is, on the other hand, critical that the measurements from the MBES is properly georeferenced to produce accurate draft measurements. This data acquisition problem, which is related to the capabilities of the mobile sensor platform, is not within the scope of this paper. Note also that since we emulate a mobile sensor moving in 3D ocean space along a repetitive path into a 2D representation, we have implemented the measurement window to re-enter in the left end of the monitoring region as it leaves at the right end to obtain periodic scanning of the interval.

As seen from Fig. 11–12, both methods capture the variation in the topography with similar performance. Since the proposed algorithms are based on truncated models, they cannot perfectly identify the real topography, and the draft estimates at the nodes, according to the performance index (33), are shown in Fig. 12 to converge to a small neighborhood around zero. Notice that the local support property of the B-splines makes the corresponding estimated topography go to zero outside the monitoring region. The Fourier method, on the other hand, is based on the assumption of a periodic signal, with period $\lambda_0 = 2\pi/\kappa_0 \approx 105 \text{ m}$, which means that the topography identified within the monitoring region will repeat itself outside the region.

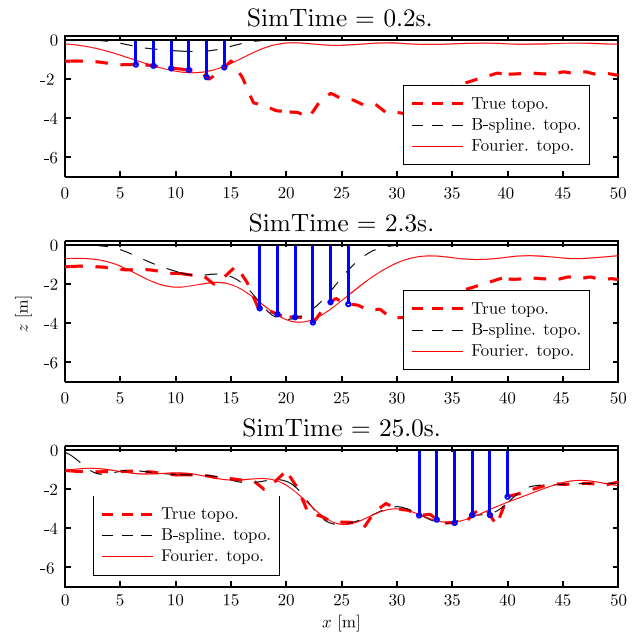


Fig. 11. Three time instants of estimation on the SCICEX-99 dataset. The blue stems show the moving measurement window y .

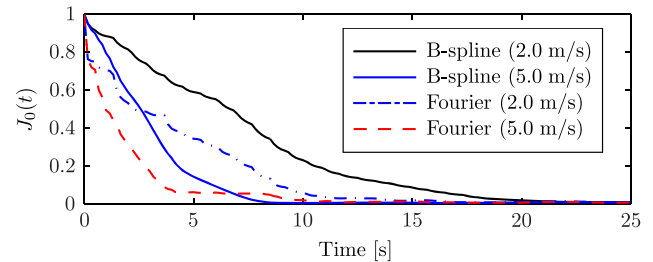


Fig. 12. Time evolutions of the performance index (33) with $v = 5.0 \text{ m/s}$ and 2.0 m/s .

An important advantage of the Fourier-based method is the robustness property explained in Section 3.1.1. To illustrate this, we have simulated the same case with the true ice drift velocity v set 50% higher than the estimated velocity \hat{v} used in the observer. The resulting response presented in Fig. 13, showing that both estimates converge, illustrates the resilience of the method to such deviation. However, even if not evident from Fig. 13, it should be mentioned that longer duration simulations have shown that the B-spline method will eventually become unstable due to such discrepancies

in the real and estimated ice drift velocities. A deeper analysis of the B-spline method is therefore needed, but not the scope of this paper.

To evaluate the filtering properties of the Fourier-based observer, we consider the case of constantly measuring only Node 1 with the estimated draft of the same node as output. For each fixed \hat{s} , the observer (24) then becomes the single input single output (SISO) linear system

$$\begin{aligned} \dot{\hat{\mathbf{d}}} &= -\mathbf{L}_d \hat{\mathbf{F}}(\hat{s}) \mathbf{W} \hat{\mathbf{F}}(\hat{s})^\top \hat{\mathbf{d}} + \mathbf{L}_d \mathbf{h}(\kappa_0, x_1, p; \hat{s}) z_1 \\ \hat{z}_1 &= \mathbf{h}(\kappa_0, x_1, p; \hat{s})^\top \hat{\mathbf{d}}, \end{aligned} \quad (40)$$

where $\hat{\mathbf{F}}(\hat{s}) \triangleq \mathbf{H}(\hat{s})\mathbf{C}$ with $\mathbf{C} = \text{diag}(1, 0, \dots, 0)$. The frequency response from the measured input z_1 to the output \hat{z}_1 of (40) is shown in Fig. 14, where the ensemble of responses corresponds to one plot for each \hat{s} -value in $\{0, 1, \dots, 105\}$ m. This shows a bandwidth slightly varying between (6–10) rad/m with efficient noise attenuation in z_1 at higher frequencies.

A qualitative comparison between the Fourier and the B-spline methods is summarized in Table I. The “computational speed” and the “simulation time” is the total run time with equivalent implementations of

Table I. Qualitative assessment of Fourier-series and B-splines.

	<i>B-spline</i>	<i>Fourier</i>
Accuracy	Good	Good
Estimator stability	Not studied	Excellent
Robust	No	Yes
Simulation time	4.4 s	2.3 s
Computational speed	Good	Better

the two methods on an HP Elitebook 8540w with 1.73 GHz CPU, using Matlab and Simulink. The values give an impression of the computational burden; however, it is possible to optimize both methods further for better performance.

With this case study, we conclude that the aim to generate a sufficiently accurate estimate of the ice topography, that can be communicated online to a remote location and reconstructed, is achieved.

V. CONCLUSIONS

In this paper an estimation design for a drifting 2D ice topography (in x - z plane) has been presented. Based on the assumption that the topography can be accurately represented by a truncated Fourier series, and given a set of measurements distributed discretely along the topography, a UGES and ISS observer was derived to estimate the topography, and a simulation illustrated its ideal performance. To quantify the performance of the proposed estimation design, we also presented an alternative estimation method, based on B-spline functions. The effectiveness of the estimation algorithms were simulated and compared on a real dataset of ice drafts taken from the underside of an ice sheet off the shores of Greenland. The results showed that both methods estimate the topography with sufficient accuracy using a low enough number of coefficients. The simulation indicated that the Fourier method has slightly faster computational speed and is more robust to uncertainties.

Through the presented problem formulation and design, this estimation problem is prepared for possibly more advanced estimator algorithms (for instance some Bayesian filtering technique such as Kalman or particle filters), for consideration of more efficient basis functions, and for extension to the 3D topography estimation case. It should be noted, though, that computational efficiency is critical and may rule out more advanced filters, especially in the 3D case. Finally, the aim is to test the system using a real underwater robot.

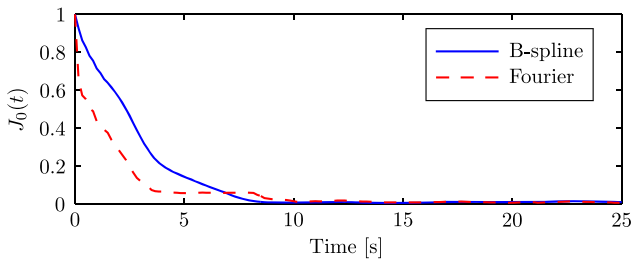


Fig. 13. Draft error convergence according to (29) when the true ice drift velocity is 50% higher than the applied estimated velocity.

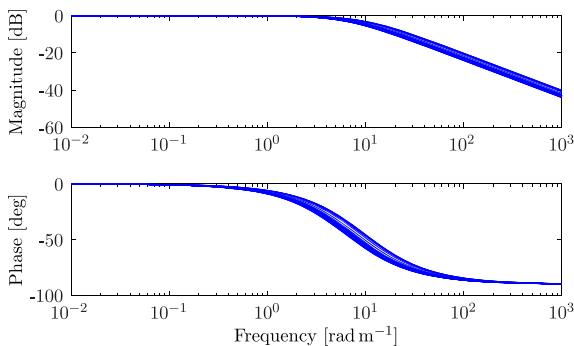


Fig. 14. Frequency responses of (40) for varying \hat{s} -values.

REFERENCES

1. Gautier, D. L., K. J. Bird, and R. R. Charpentier 'et al.', "Assessment of undiscovered oil and gas in the Arctic," *Science*, Vol. 324, No. 5931, pp. 1175–1179 (2009).
2. Moran, K., J. Backman, and J. W. Farrell, "Deepwater drilling in the Arctic Ocean's permanent sea ice," Vol. 302, *Proc. of the Int. Ocean Drilling Program*, Edinburgh, Scotland, pp. 1–13 (2006).
3. Keinonen, A., H. Wells, P. Dunderdale, R. Pilkington, G. Miller, and A. Brovin, "Dynamic positioning operation in ice, offshore Sakhalin, May–June 1999," Vol. 1, *Proc. of the Tenth Int. Offshore and Polar Engineering Conference*, Washington, USA, pp. 683–690 (2000).
4. Thomas, M., C. Geiger, and C. Kambhamettu, "High resolution (400 m) motion characterization of sea ice using ERS-1 SAR imagery," *Cold Reg. Sci. Tech.*, Vol. 52, No. 2, pp. 207–223 (2008).
5. Toutin, T. and L. Gray, "State-of-the-art of elevation extraction from satellite SAR data," *ISPRS-J. Photogramm. Remote Sens.*, Vol. 55, No. 1, pp. 13–33 (2000).
6. Haugen, J., L. Imsland, S. Løset, and R. Skjetne, "Ice observer system for ice management operations," *Proc. of the Twenty-First Int. Offshore and Polar Engineering Conference*, Maui, Hawaii, USA, pp. 1120–1126 (2011).
7. Fissel, D. B., J. R. Marko, and H. Melling, "Upward looking ice profiler sonar instruments for ice thickness and topography measurements," Vol. 3, *Oceans*, Kobe, Japan, pp. 1638–1643 (2004).
8. Fissel, D. B., J. R. Marko, E. Ross, V. Lee, R. A. J. Chave, and J. Egan, "Improvements in upward looking sonar-based sea-ice measurements: A case study for 2007 ice features in Northumberland Strait, Canada," *Oceans*, Vancouver, Canada, pp. 1–6 (2007).
9. Løset, S., K. N. Shkhinek, O. T. Gudmestad, and V. K. Høyland, "Actions from ice on arctic offshore and coastal structures," *LAN* (2006).
10. Timco, G. W. and W. F. Weeks, "A review of the engineering properties of sea ice," *Cold Reg. Sci. Tech.*, Vol. 60, No. 2, pp. 107–129 (2010).
11. Hyatt, J., M. Visbeck, R. C. Beardsley, and W. B. Owens, "Estimating sea-ice coverage, draft, and velocity in Marguerite Bay (Antarctica) using a subsurface moored upward-looking acoustic Doppler current profiler (ADCP)," *Deep Sea Res. Pt II: Topical Studies in Oceanography*, Vol. 55, No. 3–4, pp. 351–364 (2008).
12. Hoare, R., B. Danielewicz, G. Pilkington, and J. O'Rourke, "An upward-looking sonar system to profile ice keels for one year," *Oceans*, Seattle, USA, pp. 123–126 (1980).
13. Wadhams, P., "The use of autonomous underwater vehicles to map the variability of under-ice topography," *Ocean Dyn.*, Vol. 62, No. 3, pp. 439–447 (2012).
14. Fissel, D., R. A. J. Chave, and J. Buermans, "Real-time measurement of sea ice thickness, keel sizes and distributions and ice velocities using upward looking sonar instruments," *OCEANS, MTS/IEEE Biloxi - Marine Technology for Our Future: Global and Local Challenges*, Biloxi, USA, pp. 1–6 (2009).
15. Brooks, A. and T. Bailey, "HybridSLAM: Combining FastSLAM and EKF-SLAM for reliable mapping." *Algorithmic Foundation of Robotics VIII*, Springer, Berlin Heidelberg, pp. 647–661 (2009).
16. Barkby, S., S. B. Williams, O. Pizarro, and M. Jakuba, "Bathymetric particle filter SLAM using trajectory maps," *Int. J. Robot. Res.*, Vol. 31, No. 12, pp. 1409–1430 (2012).
17. Eik, K. and S. Løset, "Specifications for a subsurface ice intelligence system," *Proc. of the ASME 28th Int. Conf. on Ocean, Offshore and Arctic Engineering*, Honolulu, Hawaii, USA, pp. 103–109 (2009).
18. Akyildiz, I. F., D. Pompili, and T. Melodia, "Underwater acoustic sensor networks: research challenges," *Ad Hoc Netw.*, Vol. 3, No. 3, pp. 257–279 (2005).
19. Kinsey, J. C., R. M. Eustice, and L. L. Whitcomb, "A survey of underwater vehicle navigation: Recent advances and new challenges," *IFAC Conf. of Manoeuvring and Control of Marine Craft*, Lisbon, Portugal (2006).
20. Paull, L., S. Saeedi, M. Seto, and H. Li, "AUV navigation and localization: A review," *IEEE J. Ocean. Eng.*, Vol. 39, No. 1, pp. 131–149 (2014).
21. Jørgensen, U. and R. Skjetne, "Dynamic estimation of drifting ice topography over a 2D area using mobile underwater measurements," *Proc. of the 22nd Int. Conf. on Port and Ocean Engineering under Arctic Conditions*, Espoo, Finland (2013).
22. Jørgensen, U. and R. Skjetne, "Dynamic estimation of drifting ice topography using underwater mobile measurements," *Proc. of the 2012 American Control Conf.*, Montréal, Canada, pp. 301–306 (2012).
23. National Snow and Ice Data Center, Submarine upward looking sonar ice draft profile data and statistics (1998). Digital media, Boulder, Colorado USA: National Snow and Ice Data Center/World Data Center for Glaciology.
24. Arctic Submarine Laboratory, Arctic submarine laboratory, science ice expeditions (1999). Available

from: www.csp.navy.mil/asl/Scicex.htm [Accessed on 29 April 2013].

25. Oppenheim, A. V., A. S. Willsky, and H. Nawab, *Signals & Systems*, 2nd ed, Prentice Hall, New Jersey, USA (1996).
26. Shannon, C. E., "Communication in the presence of noise," *P. IEEE*, Vol. 72, No. 9, pp. 1192–1201 (1984).
27. Anderson, B. D. O., "Exponential stability of linear equations arising in adaptive identification," *IEEE Trans. Autom. Control*, Vol. 22, No. 1, pp. 83–88 (1977).
28. Ioannou, P. A. and J. Sun, *Robust Adaptive Control*, Prentice-Hall, New Jersey, USA (1996).
29. Khalil, H. K., *Nonlinear Systems*, third ed, Prentice Hall, New Jersey, USA (2002).
30. Brunet, F., "Contributions to Parametric Image Registration and 3D Surface Reconstruction," *Ph.D. Thesis*, Université d Auvergne (2010).



Ulrik Jørgensen received in 2010 his M.Sc. in control engineering at the department of Engineering Cybernetics, Norwegian University of Science and Technology (NTNU), Trondheim, Norway. Today, he is working towards a Ph.D. degree within the field of marine control engineering at

the Marine Technology department, NTNU. The Ph.D. is part of the KMB Arctic DP research project, which researches the possibilities for performing dynamic positioning (DP) operations in the high north. Moreover, he is currently hired as a project engineer for ICD Software AS and is working with motion compensated gangways for marine vessels. His research interests include

nonlinear motion control for single or multiple vessels, guidance and control, and Arctic dynamic positioning operations.



Roger Skjetne received in 2000 his M.Sc. degree in control engineering at the University of California at Santa Barbara and in 2005 his Ph.D. degree at the Norwegian University of Science and Technology (NTNU), for which the thesis was awarded the Exxon Mobil prize for best

Ph.D. thesis in applied research. Prior to his studies, he worked as an electrician for Aker Elektro AS on numerous oil installations for the North Sea. In 2004–2009 he was employed in Marine Cybernetics AS, working on Hardware-In-the-Loop (HIL) simulation for testing safety-critical marine control systems. From August 2009 he has held the position of Professor in Marine Control Engineering at the Department of Marine Technology at NTNU, where he presently is the leader of the research group on Marine Structures. His research interests are within Arctic stationkeeping operations and Ice Management systems for ships and rigs, environmentally robust control of shipboard electric power systems, and nonlinear control theory for motion control of single and groups of marine vessels. Roger Skjetne is project manager for the KMB Arctic DP research project, leader of the ice management work package in the CRI Sustainable Arctic Marine and Coastal Technology (SAMCoT), and associated researcher in the CoE Centre for Ships and Ocean Structures (CeSOS) and CoE Autonomous Marine Operations and Systems (AMOS).